Charge transport and recombination in wide-bandgap Y6 derivatives-based organic solar cells

Charge Transport and Recombination in Wide-Bandgap Y6 Derivatives -Based Organic Solar Cells

Yuliar Firdaus[1, 2, 4], Qiao He[3], Lia Muliani[1], Erlyta Septa Rosa[1], Martin Heeney[3], and Thomas D. Anthopoulos[2]

[1] Research Center for Electronics, National Research and Innovation Agency (BRIN), Jalan Sangkuriang Komplek LIPI Building 20 level 4, Bandung 40135 Indonesia

[2] King Abdullah University of Science and Technology (KAUST), Physical Sciences and Engineering Division (PSE), KAUST Solar Center (KSC), Thuwal 23955-6900, Saudi Arabia

[3] Department of Chemistry and Centre for Plastic Electronics, Imperial College London, London W12 0BZ, UK

[4] Author to whom any correspondence should be addressed

Email : firdaus.yuliar@gmail.com

Abstract. The power conversion efficiency of nonfullerene-based organic solar cells (OSCs) has recently exceeded 18%, thanks to the constant effort to identify the key properties governing the OSCs performance and development of better photovoltaic materials. With its superior properties, low-bandgap Y6 and its derivatives have emerged as one of the most popular nonfullerene acceptors (NFAs) for OSCs. In most cases, these low bandgap NFAs were based mainly on the most widely used and successful end-group 1,1-dicyanomethylene-3-indanone (IC). On the other hand, wide-bandgap Y6 derivatives are still scarce. Attempts to increase the NFA's bandgap by incorporating electron-rich end-groups often end up with NFAs with poor performance. In this work, we compare two wide-bandgap Y6 derivatives with different end-groups, and their distinct device performance is correlated with their charge transport and recombination properties. Electronic measurements on solar cell devices and device physics results are presented to discuss charge transport and recombination within the device.

Keywords: Organic solar cells, wide-bandgap acceptor, Y6 derivatives, charge transport, recombination

Classification numbers: 4.10, 5.01, 5.03, 5.10, 6.03

1. Introduction

Organic solar cells (OSCs) have gained the spotlight with the emergence of fused-ring nonfullerene acceptors (NFAs) Y6, and its derivatives and power conversion efficiencies (PCEs) over 18% have been reported.[1-3] The optoelectronic properties of fused-ring NFAs are greatly influenced by their end-groups. The

highly electronegative 1,1-dicyanomethylene-3-indanone (IC) is the most widely used and most successful end-group for medium and low bandgap NFAs.[4] Low-bandgap materials with absorption well matched to the solar spectrum are a general option for improving short-circuit current density and PCEs in single-junction OSCs.[5]

Recent developments in NFAs, have been focused almost exclusively on low bandgap materials (<1.6 eV), with bandgaps as low as ca. 1.0 eV has been reported, extending their absorption well into the near-infrared (NIR).[6-8] The NIR absorption could be crucial for applications such as tandem PV,[9] (semi)transparent PV,[10, 11] agrivoltaics,[12] and organic photodetectors.[13, 14] In contrast, wide-bandgap acceptors with good performance receive a lot less attention.[15, 16] Wide bandgap NFAs with high electron mobility (i.e., > 10^{-4} cm^2 V^{-1} s^{-1}) are scarce, and their development is currently needed in order to construct highly efficient multijunction or indoor OSCs.[17, 18] A wide-bandgap NFA's low electron mobility is typically due to the choice of its terminal electron-withdrawing unit. A common method to increase the NFA bandgap is by reducing the electron-pulling effect of the molecule by incorporating electron-rich groups such as rhodanine, dicyano rhodanine, cyanide, malononitrile, or 3-diethyl-2-thiobarbituric acid (TBA), which typically result in wide-bandgap NFAs with poor electron transport (<10^{-4} $cm^2V^{-2}s^{-1}$).[15, 19] Thus, understanding the key

properties that govern the performance of wide-bandgap bulk heterojunction (BHJ) OSCs is required.

In our work, we study the effect of the Y6 NFA's end-group on the transport and recombination processes that determine the device performance of Y6-based BHJ OSCs. For this purpose, we studied three A-DA'D-A -based NFAs based on IC, malononitrile (CN), and 3-diethyl-2-thiobarbituric acid (TBA) endgroups.

2. Experimental

2.1. *Materials*

PFN-Br (poly[9,9-bis(6′-bromohexyl)fluorene-alt-co-1,4-phenylene), **Y6** (2,2′-((2Z,2′Z)-((12,13-bis(2-ethylhexyl)-3,9-diundecyl-12,13-dihydro-[1,2,5]thiadiazolo[3,4-e]thieno[2,″30″:4′,5′]thieno[2′,3′:4,5]pyrrolo[3,2-g]thieno[2′,3′:4,5]thieno[3,2-b]indole-2,10-diyl)bis(methanylylidene))bis(5,6-difluoro-3-oxo-2,3-dihydro-1H-indene-2,1-diylidene))dimalononitrile), **PBDB-T** (poly[(2,6-(4,8-bis(5-(2-ethylhexyl)thiophen-2-yl)-benzo[1,2-b:4,5-b']dithiophene))-alt-(5,5-(1',3'-di-2-thienyl-5',7' bis(2-ethylhexyl)benzo[1',2'-c:4',5'-c']dithiophene-4,8-dione))]), and **PBDB-T-2F** (Poly[(2,6-(4,8-bis(5-(2-ethylhexyl-3-fluoro)thiophen-2-yl)-benzo[1,2-b:4,5-b']dithiophene))-alt-(5,5-(1',3'-di-2-thienyl-5',7'-bis(2-ethylhexyl)benzo[1',2'-c:4',5'-c']dithiophene-4,8-dione)]), and were purchased from Solarmer Materials Inc (Beijing). **PEDOT:PSS** Clevios P VP AI 4083 was purchased from Heraeus. **Y6TA** and

Y6CN acceptors were synthesized at Imperial College London. Indium tin oxide (ITO) coated glass substrates were purchased from Kintec Company (10-15 Ω/sq.)

2.2. *Thin Film Preparation and Solar Cells Fabrication*

ITO substrates were cleaned sequentially by ultra-sonication in dilute detergent solution, deionized water, acetone, and isopropyl alcohol each for 20 minutes. The substrates were then cleaned by UV-ozone treatment for 20 min. Next, a thin film of PEDOT:PSS (≈20-30 nm) was spin-coated onto the cleaned substrates and then annealed on a hot plate at 150 °C (10 min). PBDB-T-2F:Y6 was fabricated following a previous report.[5] PBDB-T:Y6 or PBDB-T:Y6TA or PBDB-T-Y6CN (ratio 1:1.5, 15.6 mg/ml in chloroform+0.5 vol% 1-chloronaphtalene) were spin-cast at speed 2500 rpm. The films were then annealed at 120°C on the hot plate for 10 minutes. A layer of 5 nm electron-transport layer (ETL) of PFN-Br was spun (0.5 mg mL^{-1} in methanol) on top of the photoactive film. Finally, 100 nm of silver (Ag) was thermally evaporated at 2×10^{-6} mbar through a 0.1 cm^2 pixel area shadow mask.

The charge carrier transport (hole and electron mobilities) of optimized neat and blend active layers were determined by fitting the dark current-voltage (J-V) of hole/electron-only devices to the space-charge-limited current (SCLC) model. *Hole-only device*: Glass/ITO/PEDOT:PSS/neat or blend film/MoO_3/Ag. First, a

PEDOT:PSS film (20-30 nm) was spin-coated at 4000 rpm for 30 s onto the ITO-coated substrate in air and then dried at 150º C for 10 min. After deposition of the neat or blend films on the PEDOT:PSS-coated substrates, MoO_3 (7 nm) and Ag (100 nm) were thermally evaporated in a vacuum chamber (base pressure of 2×10^{-6} mbar). *Electron-only device*: Glass/ITO/a-ZnO /neat or blend film/PFN-Br/Ag. The a-ZnO precursor solution was prepared following our previous report.[19, 20] The remaining layers were deposited following the same procedure of the OSC devices described above.

Neat and blend films for characterizations (PESA, UV-vis, photoluminescence (PL)) were prepared following solar cell fabrication steps and the film was deposited onto quartz substrates in glovebox. Photoelectron spectroscopy in air (PESA) measurements were recorded using a Riken Keiki PESA spectrometer (Model AC-2) using samples prepared on glass substrates. UV-vis spectra of films on glass were measured with a Cary 5000. Steady-state PL spectra were measured with a HORIBA-fluoroMax-4 in 30° reflection geometry.

2.3. *Device Characterizations*

J–V and External quantum efficiency (EQE) measurements of solar cells were performed in an N_2 filled glove box following our previous report.[19] Light-intensity dependence measurements (J-V, TPV, CE, TPC) were performed with PAIOS instrumentation (Fluxim) following our previous report.[20]

3. Results and Discussion

3.1. *Material and Device Performance*

The chemical structure of the polymer donor materials PBDB-T, and PBDB-T-2F, and nonfullerene acceptors Y6, Y6TA, Y6CN discussed in this work are shown in Figure 1a, while the films' UV-vis absorption spectra are presented in Figure 1b. Notably, the donor materials and Y6TA, Y6CN acceptors show overlapping absorption across the visible-wavelength range (300-700 nm). In contrast, Y6 mainly absorbs in the near-infrared (NIR) spectral range of 600-1000 nm. The optical bandgap (E_{opt}) of the donors, as measured from the onset of absorption, was 1.8 eV and 1.85 eV for PBDB-T, and PBDB-T-2F, respectively. Additionally, the E_{opt} of the acceptors is 1.33 eV, 1.65 eV, and 1.97 eV for Y6, Y6TA, and Y6CN. The ionization energy (IE) of PBDB-T, PBDB-T-2F, Y6, Y6TA, and Y6CN, inferred from photoelectron spectroscopy in air (PESA, Figure 1c), were -5.05 eV, -5.16 eV, -5.65 eV, -5.72 eV, and -5.80 eV, respectively. Based on these results, the energy level of the donors and acceptors is summarized in Figure 1d. Efficient charge dissociation at the donor-acceptor interface could be expected based on the IE offset values between the polymer donors (PBDB-T and PBDB-T-2F) and the acceptors (Y6, Y6TA, and Y6CN).[21]

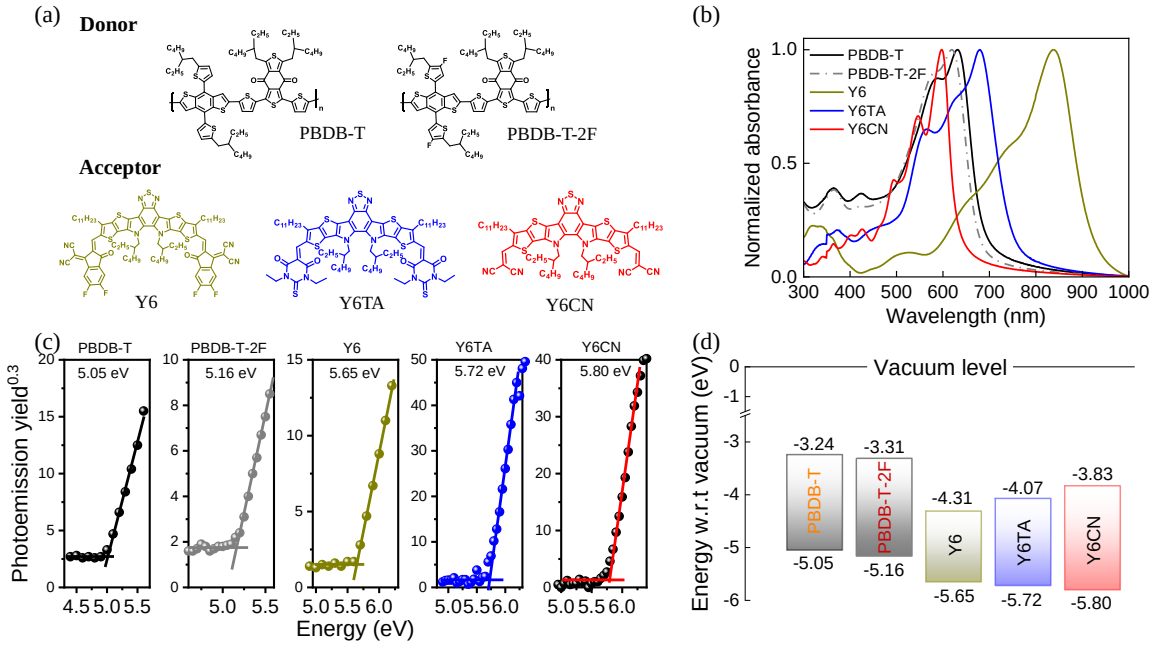

FIGURE 1. (a) Chemical structures of the polymer donors (PBDB-T, and PBDB-T-2F) and NFAs (Y6, Y6TA, and Y6CN) used in this work, (b) Normalized absorbance of the donor and acceptor films, (c) PESA curves for PBDB-T-2F, PBDB-T, Y6TA, Y6CN, and Y6 neat films. PESA-inferred ionization energies (IEs) are reported on the plots. (d) The IE values obtained from PESA measurements (Figure 1c) and IE + optical gap (E_{opt}), E_{opt} were estimated from the inset of the UV-Vis of neat film absorption spectra.

To test the performance of Y6TA and Y6CN NFAs in BHJ OSCs, we mixed them with the PBDB-T or PBDB-T-2F polymer donors and fabricated conventional BHJ OSC cells consisting of glass/ITO/PEDOT:PSS/photoactive layer/PFN-Br/Ag (Figure 2a). For comparison, we also fabricated OSC devices based on the Y6 acceptor. The photoactive layers were spin-cast from chloroform solutions, and we obtained films with thickness between 100-140 nm.

Table 1. Photovoltaic parameters of Y6, Y6TA, Y6CN -based OSC. The statistics were at least from 10 cells. Cells based on Y6TA and Y6CN were annealed at 120 °C, and 100 °C for Y6-based devices.

Blend	**V_{OC} (V)**	**J_{SC} (mA cm^{-2})**	**$J_{SC,cal}$* (mA cm^{-2})**	**FF (%)**	**PCE_{avg} (%)**	**PCE_{max} (%)**
PBDB-T-2F:Y6	0.84±0.006	25.2±0.17	24.6	70.8±0.77	15.1±0.18	15.4
PBDB-T-2F:Y6TA	1.13±0.002	4.0±0.09	-	32.1±0.21	1.4±0.03	1.5
PBDB-T-2F:Y6CN	1.27±0.010	4.3±0.07	-	34.5±0.84	1.9±0.07	2.0
PBDB-T:Y6	0.71±0.003	23.9±0.69	-	59.6±1.60	10.2±0.23	10.8
PBDB-T:Y6TA	1.04±0.006	13.0±0.36	12.6	53.4±0.67	7.2±0.19	7.5
PBDB-T:Y6CN	1.13±0.02	8.3±0.13	8.9	42.2±0.76	4.0±0.10	4.1

*The EQE-integrated J_{SC} obtained from Figure 2d.

Table 1 summarized the open-circuit voltage (V_{OC}), short-circuit current density (J_{SC}), fill-factor (FF), and PCE of optimized OSCs. The current-voltage (J-V) curves of OSC cells recorded under the simulated solar illumination are shown in Figure 2b-c. In close agreement with the previous report,[5] devices based on PBDB-T-2F:Y6 exhibit an average PCE value of 15.4% with a J_{SC} of 25.2 mAcm^{-2}, V_{OC} of 0.84 V, and FF of 70.8%. On the other hand, Y6TA and Y6CN -based devices yielded markedly lower PCE. Y6TA and Y6CN NFAs only reach maximum PCE of 1.5% and 2%, respectively, when blended with PBDB-T-2F, mainly due to its much lower J_{SC} and FF (Figure 2b, Table 1). The PCE increase up to 7.5% and 4.1% for Y6TA, and Y6CN, respectively, when they are blended with the PBDB-T donor, which were attributed to the increase of J_{SC} and FF (Figure 2c, Table 1). We also fabricated devices based on the PBDB-T:Y6

blend and average PCE of 10.2% was obtained with a J_{SC} of 23.9 $mAcm^{-2}$, V_{OC} of 0.71 V, and FF of 59.6%. The lower V_{OC} of PBDB-T:Y6 devices compared to PBDB-T:Y6TA and PBDB-T:Y6CN is following the trend in energy level, particularly values of IE+E_{opt} (Figure 1d). The external quantum efficiency (EQE) spectra of optimized PBDB-T-2F:Y6, PBDB-T:Y6TA, and PBDB-T:Y6CN BHJ cells are shown in Figure 2d. In agreement with the absorption spectra of PBDB-T and Y6CN (Figure 1b), the Y6CN-based devices show photocurrent response in the range of 300-700 nm. On the other hand, the EQE spectra extend up to 750 nm and 950 nm for the PBDB-T:Y6TA and PBDB-T-2F:Y6 based cells. Additionally, PBDB-T-2F:Y6 -based devices exhibit higher EQE, nearly 80%, whereas the EQEs of PBDB-T:Y6TA and PBDB-T:Y6CN are around 60%.

3.2. *Charge Transport*

To understand the difference in performance between PBDB-T-2F:Y6, PBDB-T:Y6TA, and PBDB-T:Y6CN devices, we studied the charge transport by space-charge limited current (SCLC) measurements using carefully engineered carrier-selective devices. We measured the hole mobilities of neat PBDB-T, PBDB-T-2F, as well as the electron mobilities of neat Y6, Y6TA, Y6CN. Additionally, we measured the hole and electron mobilities of PBDB-T-2F:Y6, PBDB-T:Y6, PBDB-T:Y6TA, PBDB-T:Y6CN blends.

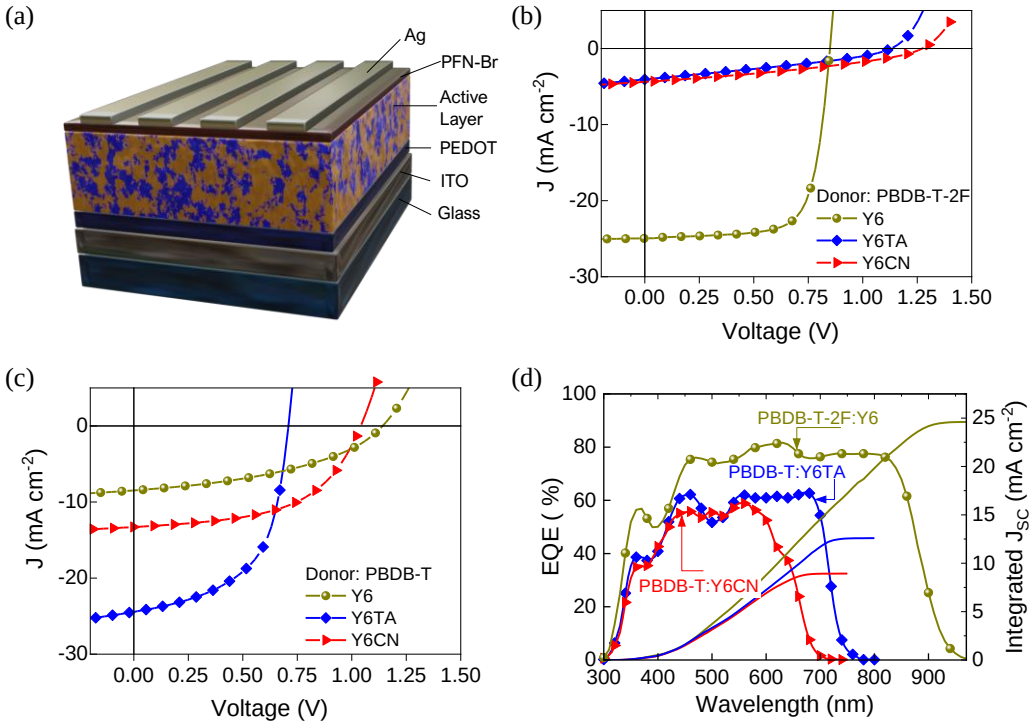

FIGURE 2. (a) Device structure of BHJ OSC fabricated in this work. (b) J-V characteristics of PBDB-T-2F -based OSC cells. (c) J-V curves of PBDB-T -based OSC cells measured under simulated solar illumination (1 sun, AM1.5G). (d) Corresponding EQE spectra of the optimized OSC devices shown in (b) and (c).

A trap-free SCLC could be characterized by the Mott-Gurney square law:[22]

$$J = \frac{9}{8}\varepsilon\mu\frac{(V - V_{bi})^2}{d^3} \quad (1)$$

where J is the current density, ε is the permittivity, μ is the charge-carrier mobility, V_{bi} is the built-in voltage due to asymmetric work function of the electrodes, V is the applied voltage, and d is the layer thickness. Two important criteria need to be fulfilled, so the injected hole/electron currents fulfill space-charge limited condition: the current scales inversely with layer thickness to the third power, and

the current depends quadratically on voltage ($\boldsymbol{J \propto V^2}$, or m=2). However, the current shows stronger voltage dependence for trap-limited charge transport, which follows a power-law relation $\boldsymbol{J \propto V^m}$, m>2.[22]

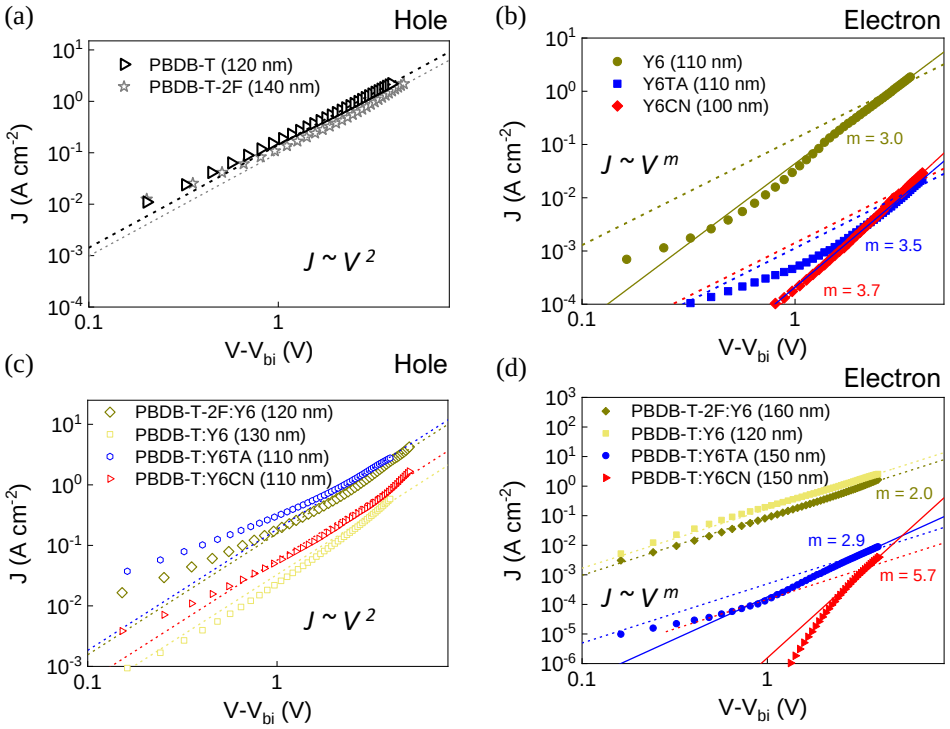

FIGURE 3. Experimental dark J-V for (a) hole-only diodes of neat PBDB-T, and PBDB-T-2F polymer donor films, (b) electron-only diodes of neat Y6, Y6TA, and Y6CN NFA films, (c) hole-only diodes and (d) electron-only diodes of PBDB-T-2F:Y6, PBDB-T:Y6, PBDB-T:Y6TA, and PBDB-T:Y6CN. The experimental data were fitted using the trap-free SCLC model/equation 1 (dashed lines) and trap-limited SCLC model (solid lines).

Figure 3a shows the hole current densities of neat PBDB-T and PBDB-T-2F, which depend quadratically on voltage and can be fitted with equation 1. The hole/electron mobilities obtained from the fitting are summarized in Table 2. We also include the adjusted-R^2 (adj.R^2) in Table 2 to describe the quality of the fits. An adjusted-R^2 value of 1 indicates a model which perfectly predicts the

experimental data. Only the fitting for electron current of Y6CN and PBDB-T:Y6CN devices exhibit adj.R^2 less than 0.9, indicating their poor fitting to the Mott-Gurney equation. Our analyses indicate that the hole mobilities of PBDB-T and PBDB-T-2F films fall within the same range, with estimated values of 7.1×10^{-4} and 7.8×10^{-4} $cm^2V^{-1}s^{-1}$, respectively. In comparison, neat Y6, Y6TA, and Y6CN films exhibit electron current density-voltage characteristics with the slope (*m*) larger than 2, indicating trap-limited transport (see Figure 3b). The electron current density of Y6 is two orders of magnitude higher than Y6TA and Y6CN. As a result, the electron mobilities of Y6TA and Y6CN are ~4×10^{-6} $cm^2V^{-1}s^{-1}$, which is two orders of magnitude lower than Y6 (5×10^{-4} $cm^2V^{-1}s^{-1}$, Table 2). In optimized BHJ active layers, hole mobilities estimated for PBDB-T:Y6TA and PBDB-T-2F:Y6 active layers is ~ 7×10^{-4} $cm^2V^{-1}s^{-1}$, nearly 4× as high as those for PBDB-T:Y6 and PBDB-T:Y6CN (Table 2). The hole mobility of PBDB-T:Y6 is four times lower than the hole mobility of PBDB-T-2F:Y6 devices. Additionally, the electron mobility of devices based on the fluorinated polymer is higher (1.1×10^{-3} $cm^2V^{-1}s^{-1}$) than devices with PBDB-T (8.3×10^{-4} $cm^2V^{-1}s^{-1}$), which could be the reason for the lower performance of PBDB-T:Y6 devices. The lower hole and electron mobility of PBDB-T:Y6 blend films could be due to non-optimal donor/acceptor phase separation in agreement with the lower FF of this system. Interestingly, Y6-based blend active layers exhibit trap-free transport and trap-

limited for the Y6TA and Y6CN blend films. The electron mobility estimated for PBDB-T:Y6TA and Y6CN is two orders of magnitude lower than Y6-based blend films. The imbalance between hole and electron mobilities in the PBDB-T:Y6TA or Y6CN blend films could be the reason for significant charge recombination in those devices, limiting the FF and J_{SC}.

Table 2. Charge mobilities of neat polymer donors, acceptors and blend films discussed in this work. All the mobility values were inferred from the trap-free SCLC model (Mott-Gurney equation, Equation 1).

Active-Layer	**Hole Mobility ($cm^2V^{-1}s^{-1}$)**	**Adj. R^2**	**Electron Mobility ($cm^2V^{-1}s^{-1}$)**	**Adj. R^2**
PBDB-T-2F	7.8×10^{-4}	0.996	-	-
PBDB-T	7.1×10^{-4}	0.999	-	-
Y6	-	-	$<5.0\times10^{-4}$	0.948
Y6TA	-	-	$<4.3\times10^{-6}$	0.922
Y6CN	-	-	$<4.1\times10^{-6}$	0.894
PBDB-T-2F:Y6	7.7×10^{-4}	0.994	1.1×10^{-3}	0.992
PBDB-T:Y6	2.1×10^{-4}	0.980	8.3×10^{-4}	0.999
PBDB-T:Y6TA	7.0×10^{-4}	0.991	4.8×10^{-6}	0.961
PBDB-T:Y6CN	2.2×10^{-4}	0.973	$<1.4\times10^{-6}$	0.738

3.3. *Charge Recombination*

Information on charge recombination across the OSC devices can be inferred from different measurement techniques. Steady-state photoluminescence (PL) measurements were used to investigate exciton dynamics. PL quenching analysis is typically used to measure excitons separation at the donor-acceptor interfaces,

which for highly efficient BHJ OSCs, the PL quenching is typically exhibiting nearly 100%. The neat and blend films absorbance (Figure 4a) was also taken to account for the PL spectra correction. The excitation wavelength for the PL measurements was 550 nm which exclusively probed the polymer donor domains for Y6-based blend films and both donor-acceptor domains for Y6TA, Y6CN -based blend films. Both PBDB-T and PBDB-T-2F's PL are nearly quenched in the presence of Y6, as illustrated in Figure 4b (quenching efficiencies are 99% and 94%). On the other hand, the quenching efficiencies are lower in Y6TA and Y6CN (85% and 62%), which demonstrate exciton dissociation losses in agreement with the low J_{SC} values in these systems.

The impact of NFA's end-group on charge recombination in BHJ OSCs was investigated. Figure 5a shows V_{OC} *vs.* light intensity variation in a natural logarithmic scale with data fitted to:

$$\boldsymbol{V_{OC} \propto S\frac{kT}{q}\ln(I)} \tag{2}$$

where *k*, *T*, and *q* are the Boltzmann constant, the temperature in *K*, and the elementary charge, respectively. The parameter *S* could indicate the presence/absence of carrier traps in the solar cell devices. If trap-assisted recombination in the bulk is involved, a slope in the plot of V_{OC} *vs*. light intensity

greater than 1kT/q will be observed.[23, 24] In addition, the slope lower than 1kT/q could also mean the presence of surface traps.[25] Figure 5a shows that the V_{OC} *vs*. light intensity plot for Y6TA and Y6CN-based device presents a slope of 1.23kT/q and 1.26kT/q, which is higher than 1.18 kT/q for Y6-based devices, which suggest lower trap-assisted recombination in Y6-based devices.

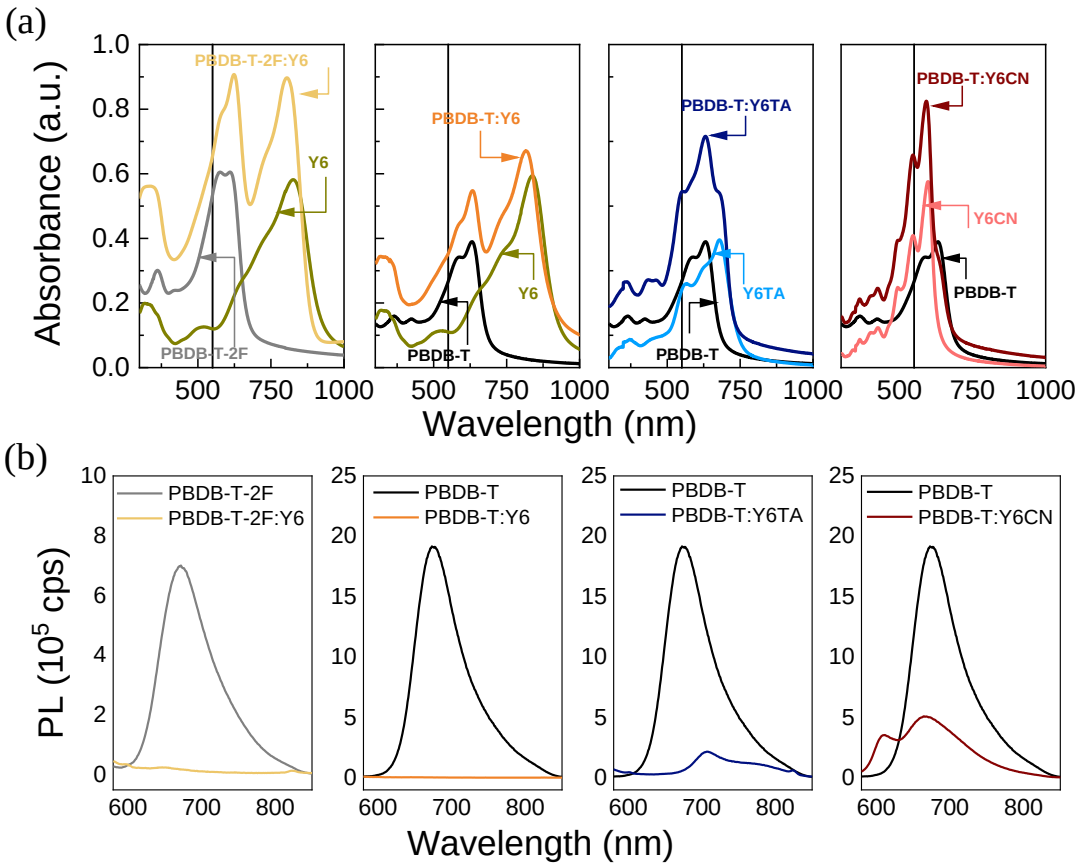

FIGURE 4. (a) Absorbance spectra of neat polymer donors, neat NFAs, and blend films used to measure PL spectra shown in Figure 4b. (b) PL quenching of PBDB-T or PBDB-T-2F in the presence of the NFAs (Y6, Y6TA, and Y6CN). Excitation at 550 nm as highlighted by the vertical line. The PL spectra is corrected with the absorption level at excitation wavelength.

Next, we performed transient-photovoltage (TPV) measurements, measured under open-circuit conditions. The charge carrier lifetime (τ) was extracted from the TPV small perturbation decay dynamics using mono-exponential fits for different light intensities (3-100% of the maximum light intensity of 200 mW cm^{-2}).[20] Figure 5b shows that the devices with Y6TA and Y6CN show higher τ values in most intensity range than the Y6-based devices. The longer τ in Y6TA and Y6CN -based devices could be due to the presence of trapping-and-release events, which slow down the actual recombination process.

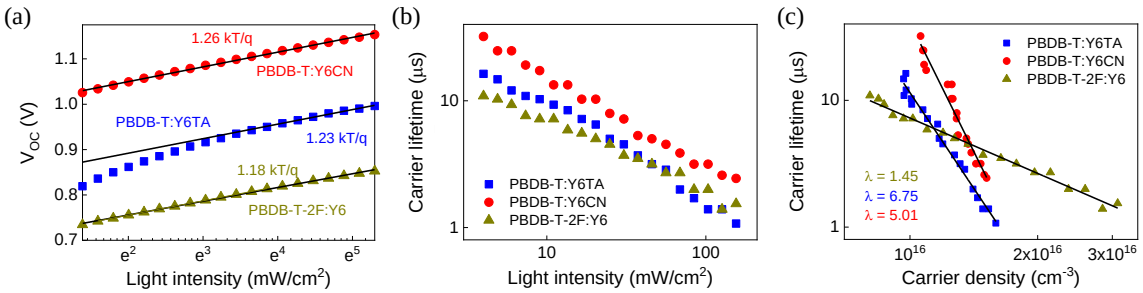

FIGURE 5. Light intensity dependence of (a) V_{OC}, and (b) charge carrier lifetime. (c) Charge carrier lifetime obtained from TPV measurements plotted as a function of charge carrier density obtained from charge-extraction (CE) measurements.

We also performed charge-extraction (CE) measurements on the same devices at the same range of light intensities from which the carrier densities were inferred. As shown in Figure 5c, Y6TA and Y6CN -based devices exhibit lower carrier densities than Y6-devices, particularly at higher intensities. Recombination rate constant (see the derivation in the Supporting Information, SI):

$$k_{rec} = \frac{1}{(\lambda + 1)n\tau} \tag{3}$$

then can be inferred from the carrier lifetime and densities, where λ is the recombination order determined from the analyses presented in Figure 5c.

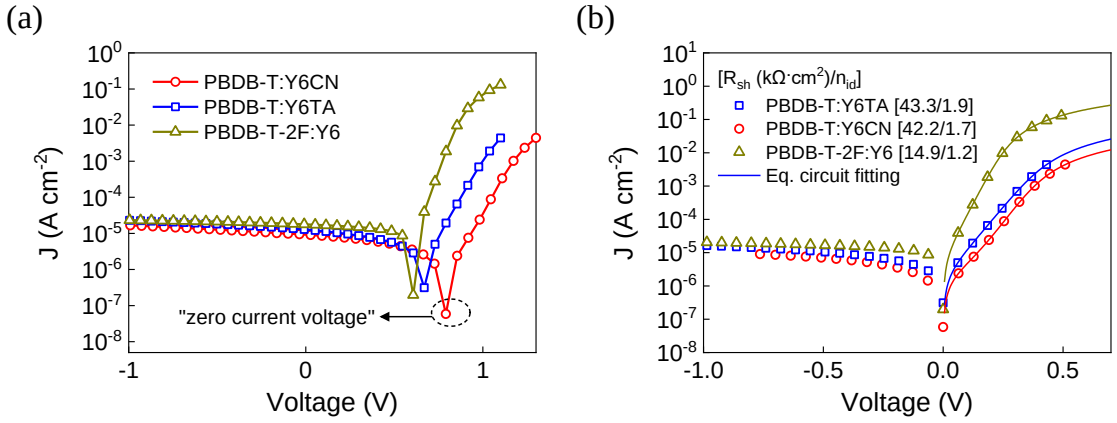

FIGURE 6. (a) The dark J-V curves of PBDB-T:Y6TA, PBDB-T:Y6CN, PBDB-T-2F:Y6 OSC devices. (b) The dark J-V after shifting the "zero current voltage" to zero applied voltage in order to calculate the shunt resistance using an equivalent circuit model.[26] The figure legend also show the calculated shunt resistance, R_{sh}, in kΩ·cm^2 and ideality factor (n_{id}) obtained from the equivalent circuit model fitting (equation 4).

While the recombination rate constant of Y6-based devices are substantially lower than Y6TA and Y6CN -based devices, the recombination orders of the latter two devices are uncommonly high (>3). The λ of 3 could still be explained by Auger recombination, usually observed under high charge carrier densities conditions, which is irrelevant for OSCs under realistic operating conditions.[27] However, light intensity-dependent measurements could be affected by the

device's leakage current or shunt resistance (R_{sh}).[28] For OSC devices with low R_{sh}, the leakage current may significantly distort J-V measurements performed at light intensities less than one sun.[28] In order to examine the leakage current in our devices, their dark J-V was measured and are depicted in Figure 6a. The region that accounts for leakage currents around "zero-current voltage" appears to be similar in current (10^{-7}-10^{-5} A·cm^{-2}) for all devices. To extract R_{sh}, we fit the dark J-V curves with equivalent circuit model, which account for shunt resistance (R_{sh}) and series resistance (R_S):[26]

$$\boldsymbol{J = J_0\left[exp\left(\frac{q(V - JAR_S}{n_{id}kT}\right) - 1\right] + \frac{V - JAR_S}{AR_{sh}} - J_{ph}} \quad (4)$$

where A is the area of the device, k is the Boltzmann constant, T is the temperature, n_{id} is the diode ideality factor, and J_{ph} is photocurrent. From the fitting to this model (Figure 6b), R_{sh} inferred from the model found to be ~15 kΩ·cm^2 for PBDB-T-2F:Y6, which is lower than the R_{sh} of PBDB-T:Y6TA and PBDB-T:Y6CN (~40 kΩ·cm^2), indicating that their R_{sh} does not cause the large λ (>3) for the latter two devices. From the fitting of dark J-V curves, we could also extract the information about ideality factor (n_{id}), which characterizes recombination-process order, of 1.9, 1.7, and 1.2 for Y6TA, Y6CN, and Y6-based devices, respectively.

Additionally, we observed that the deflection voltage of the dark J-V (namely "zero-current voltage" in Figure 6a) is not zero for all three devices and increasing toward higher voltage from PBDB-T-2F:Y6, PBDB-T:Y6TA, and PBDB-T:Y6CN. The "zero-current voltage" shifting in dark J-V curves has been reported recently and attributed to the increase in device capacitance.[29] This trend could explain the high λ from TPV+CE found in PBDB-T:Y6TA and PBDB-T:Y6CN. Tress et. al.[30] recently reported that in devices with high capacitance and low mobility, the time constant (τ) obtained from TPV measurements does not describe recombination dynamics but RC times for charging the electrodes (R_s: series resistance, C: geometric capacitance). To verify if the "zero-current voltage" shift is due to the increase in device capacitance, we have performed voltage pulse measurement (see Supporting Information for the measurement details). The current transient of PBDB-T-2F:Y6, PBDB-T:Y6TA, and PBDB-T:Y6CN devices obtained from this measurement is shown in Figure S2. From the measurement analysis, PBDB-T-2F:Y6 device exhibits a geometric capacitance of 2.47 nF, which increases to 3.16 nF and 2.83 nF for PBDB-T:Y6TA and PBDB-T:Y6CN devices, respectively. Additionally, the RC time of Y6TA-based and Y6CN-based devices are 0.18 µs and 0.16 µs, which is higher than for PBDB-T-2F:Y6 devices (0.13 µs). However, the measured RC times and the geometric capacitance of Y6, Y6TA, and Y6CN -based devices (increase with

order: Y6, Y6CN, Y6TA, with no big difference between Y6CN and Y6TA) could not fully explain the "zero-current voltage" shift trend (shift with order: Y6, Y6TA, Y6CN). Further investigation in this particular aspect is still required, which is beyond the scope of this work.

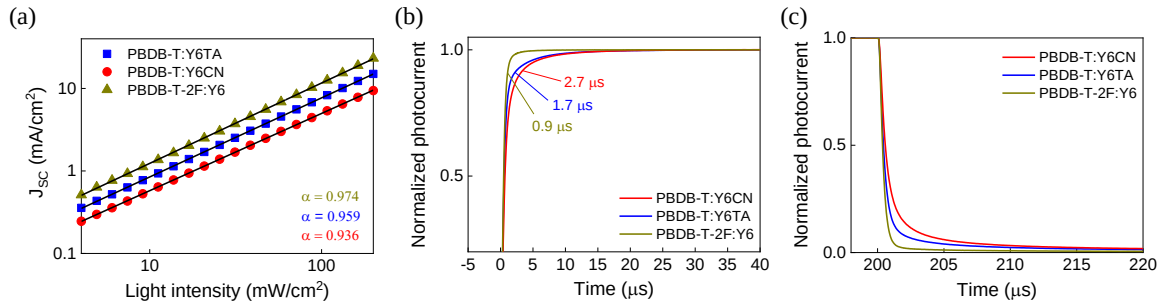

FIGURE 7. (a) Light intensity dependence of J_{SC}. Normalized transient short-circuit current (b) turn-on dynamics, and (c) turn-off dynamics, obtained from TPC measurements in response to a 200 μs white light (LED) pulse.

We also measured the light-intensity dependence of J_{SC} to qualitatively examine the bimolecular recombination losses under short-circuit conditions in the BHJ cells. The J_{SC} and light intensity (P_{light}) relationship can be described as

$$\boldsymbol{J_{SC} \propto (P_{light})^{\alpha}} \quad (5)$$

Here, α would be equal to 1 if all dissociated charge carriers are extracted at the corresponding electrodes without bimolecular recombination, while $\alpha < 1$ suggests the presence of bimolecular recombination.[23] For OSC cells with Y6 NFA, an α value of 0.974 is obtained, compared to 0.959 and 0.936 for devices with Y6TA and Y6CN, respectively (Figure 7a). This indicates that Y6TA and Y6CN can extract out photogenerated charges less efficiently and have more

bimolecular recombination compared to devices based on Y6 acceptor. The deviation from unity for α can also stem from imbalanced mobilities.[23, 31, 32] Indeed, the values of α for the three systems are strongly correlated with their mobilities (see Table 2).

Next, we performed transient photocurrent (TPC) measurement under short-circuit conditions to get information on the trapping/detrapping process and the impact of charge transport.[33] Here the OSC device is excited by a square-shaped light pulse long enough for the current density to reach a steady state. The time taken for the device to reach a steady-state provides insights into the turn-on and turn-off dynamics, which could indicate the difference in charge transport.[34] Figure 7b,c shows the current response of PBDB-T:Y6, PBDB-T:Y6TA, and PBDB-T:Y6CN BHJ cells upon excitation with a white light pulse intensity of ~100 $mWcm^{-2}$. As shown in Figure 7b, the rise time (defined as the time taken to rise from 10% to 90% of the maximum current amplitude), is increased from 0.9 µs for the Y6-based device to 1.7 µs and 2.7 µs for the Y6TA and Y6CN -based devices. Moreover, the turn-off characteristics (Figure 7c) of the measured photocurrent for the Y6TA and Y6CN cells show a characteristics tail indicative of a lower charge carrier mobilities in those devices.[34]

4. Conclusion

In summary, we have elucidated the origin of the significantly reduced performance of wide bandgap Y6TA and Y6CN -based BHJ solar cells compared to the reference low-bandgap Y6-based solar cells. The combination of different characterization techniques showed that the performance reduction observed in the wide-bandgap NFA-based solar cells result primarily from: i) poor electron transport in neat and blend Y6TA and Y6CN -based active layers ~ 10^{-6} $cm^2V^{-1}s^{-1}$, which is two orders of magnitude lower than the reference Y6-based devices (>10^{-4} $cm^2V^{-1}s^{-1}$); ii) lower PL quenching efficiencies in the case of PBDB-T:Y6TA and PBDB-T:Y6CN blend films (85%, and 62%) demonstrating higher exciton dissociation losses in comparison to PBDB-T:Y6 (PLQ ~ 100%); iii) higher bimolecular and trap-assisted recombination as well as lower charge carrier density.

Acknowledgments

This publication is based upon work supported by the King Abdullah University of Science and Technology (KAUST) Office of Sponsored Research (OSR) under Award No: OSR-2018-CARF/CCF-3079; and Program Riset Nasional (PRN) from the Indonesian Ministry of Research and Technology 2020 under contract no. 141/E1/PRN/2020.

References

[1] Lin Y, Magomedov A, Firdaus Y, Kaltsas D, El-Labban A, Faber H, Naphade DR, Yengel E, Zheng X, Yarali E, Chaturvedi N, Loganathan K, Gkeka D, AlShammari SH, Bakr OM, Laquai F, Tsetseris L, Getautis V, Anthopoulos TD 2021 *ChemSusChem* 14(17) 3569-78.

[2] Lin Y, Nugraha MI, Firdaus Y, Scaccabarozzi AD, Aniés F, Emwas A-H, Yengel E, Zheng X, Liu J, Wahyudi W, Yarali E, Faber H, Bakr OM, Tsetseris L, Heeney M, Anthopoulos TD 2020 *ACS Energy Lett.* 5(12) 3663-71.

[3] Lin Y, Firdaus Y, Isikgor FH, Nugraha MI, Yengel E, Harrison GT, Hallani R, El-Labban A, Faber H, Ma C, Zheng X, Subbiah A, Howells CT, Bakr OM, McCulloch I, Wolf SD, Tsetseris L, Anthopoulos TD 2020 *ACS Energy Lett.* 5(9) 2935-44.

[4] Huang J, Tang H, Yan C, Li G 2021 *Cell Rep. Phys. Sci,* 2(1) 100292.

[5] Yuan J, Zhang Y, Zhou L, Zhang G, Yip H-L, Lau T-K, Lu X, Zhu C, Peng H, Johnson PA, Leclerc M, Cao Y, Ulanski J, Li Y, Zou Y 2019 *Joule* 3(4) 1140-51.

[6] Lee J, Ko S-J, Seifrid M, Lee H, McDowell C, Luginbuhl BR, Karki A, Cho K, Nguyen T-Q, Bazan GC 2018 *Adv. Energy Mater.* 8(26) 1801209.

[7] Lee J, Ko S-J, Seifrid M, Lee H, Luginbuhl BR, Karki A, Ford M, Rosenthal K, Cho K, Nguyen T-Q, Bazan GC 2018 *Adv. Energy Mater.* 8(24) 1801212.

[8] Lee J, Ko S-J, Lee H, Huang J, Zhu Z, Seifrid M, Vollbrecht J, Brus VV, Karki A, Wang H, Cho K, Nguyen T-Q, Bazan GC 2019 *ACS Energy Lett.* 4(6) 1401-9.

[9] Yao H, Chen Y, Qin Y, Yu R, Cui Y, Yang B, Li S, Zhang K, Hou J 2016 *Adv. Mater.* 28(37) 8283-7.

[10] Brus VV, Lee J, Luginbuhl BR, Ko S-J, Bazan GC, Nguyen T-Q 2019 *Adv. Mater.* 31(30) 1900904.

[11] Kini GP, Jeon SJ, Moon DK 2021 *Adv. Funct. Mater.* 31(15) 2007931.

[12] Meitzner R, Schubert US, Hoppe H 2021 *Adv. Energy Mater.* 11(1) 2002551.

[13] Wang C, Zhang X, Hu W 2020 *Chem. Soc. Rev.* 49(3) 653-70.

[14] Huang J, Lee J, Vollbrecht J, Brus VV, Dixon AL, Cao DX, Zhu Z, Du Z, Wang H, Cho K, Bazan GC, Nguyen T-Q 2020 *Adv. Mater.* 32(1) 1906027.

[15] Firdaus Y, He Q, Lin Y, Nugroho FAA, Le Corre VM, Yengel E, Balawi AH, Seitkhan A, Laquai F, Langhammer C, Liu F, Heeney M, Anthopoulos TD 2020 *J. Mater. Chem.* 8(3) 1164-75.

[16] Firdaus Y, Le Corre VM, Khan JI, Kan Z, Laquai F, Beaujuge PM, Anthopoulos TD 2019 *Adv. Sci.* 6(9) 1802028.
[17] Firdaus Y, Ho CHY, Lin Y, Yengel E, Le Corre VM, Nugraha MI, Yarali E, So F, Anthopoulos TD 2020 *ACS Energy Lett.* 5(12) 3692-701.
[18] Cui Y, Wang Y, Bergqvist J, Yao H, Xu Y, Gao B, Yang C, Zhang S, Inganäs O, Gao F, Hou J 2019 *Nat. Energy* 4(9) 768-75.
[19] Wang K, Firdaus Y, Babics M, Cruciani F, Saleem Q, El Labban A, Alamoudi MA, Marszalek T, Pisula W, Laquai F, Beaujuge PM 2016 *Chem. Mater.* 28(7) 2200-8.
[20] Firdaus Y, Maffei LP, Cruciani F, Müller MA, Liu S, Lopatin S, Wehbe N, Ndjawa GON, Amassian A, Laquai F, Beaujuge PM 2017 *Adv. Energy Mater.* 7(21) 1700834.
[21] Karuthedath S, Gorenflot J, Firdaus Y, Chaturvedi N, De Castro CSP, Harrison GT, Khan JI, Markina A, Balawi AH, Peña TAD, Liu W, Liang R-Z, Sharma A, Paleti SHK, Zhang W, Lin Y, Alarousu E, Anjum DH, Beaujuge PM, De Wolf S, McCulloch I, Anthopoulos TD, Baran D, Andrienko D, Laquai F 2021 *Nat. Mater.* 20(3) 378-84.
[22] Kotadiya NB, Mondal A, Blom PWM, Andrienko D, Wetzelaer G-JAH 2019 *Nat. Mater.* 18(11) 1182-6.
[23] Koster LJA, Mihailetchi VD, Xie H, Blom PWM 2005 *Appl. Phys. Lett.* 87(20) 203502.
[24] Lin Y, Adilbekova B, Firdaus Y, Yengel E, Faber H, Sajjad M, Zheng X, Yarali E, Seitkhan A, Bakr OM, El-Labban A, Schwingenschlögl U, Tung V, McCulloch I, Laquai F, Anthopoulos TD 2019 *Adv. Mater.* 31(46) 1902965.
[25] Vollbrecht J, Brus VV 2020 *Org. Electron.* 86 105905.
[26] Mazzio KA, Luscombe CK 2015 *Chem. Soc. Rev.* 44(1) 78-90.
[27] Vollbrecht J, Brus VV 2021 *Energies* 14(16) 4800.
[28] Proctor CM, Nguyen T-Q 2015 *Appl. Phys. Lett.* 106(8) 083301.
[29] Zhao Z, Wang J, Xu C, Yang K, Zhao F, Wang K, Zhang X, Zhang F 2020 *J. Phys. Chem. Lett.* 11(2) 366-73.
[30] Wang ZS, Ebadi F, Carlsen B, Choy WCH, Tress W 2020 *Small Methods* 4(9) 2000290.
[31] Cowan SR, Banerji N, Leong WL, Heeger AJ 2012 *Adv. Funct. Mater.* 22(6) 1116-28.
[32] Vollbrecht J, Lee J, Ko S-J, Brus VV, Karki A, Le W, Seifrid M, Ford MJ, Cho K, Bazan GC, Nguyen T-Q 2020 *J. Mater. Chem. C* 8(43) 15175-82.
[33] Hwang I, Greenham NC 2008 *Nanotechnology* 19(42) 424012.
[34] Neukom M, Züfle S, Jenatsch S, Ruhstaller B 2018 *Sci. Technol. Adv. Mater.* 19(1) 291-316.